Draft version February 5, 2026
Typeset using LaTeX **twocolumn** style in AASTeX631

PIC simulations of nonrelativistic high-Mach-number oblique shocks propagating in a turbulent medium

Karol Fulat [1], Eloise Moore [2], Mahmoud Alawashra [3], Michelle Tsirou [4], Artem Bohdan [5], Takanobu Amano [6] and Martin Pohl [2,3]

[1] *Department of Astronomy, University of Wisconsin-Madison, Madison, WI 53706, USA*
[2] *Institute of Physics and Astronomy, University of Potsdam, D-14476 Potsdam, Germany*
[3] *Deutsches Elektronen-Synchrotron DESY, Platanenallee 6, 15738 Zeuthen, Germany*
[4] *Institute of Physics of the Czech Academy of Sciences, Prague, 182 00, Czechia*
[5] *Max-Planck-Institut für Plasmaphysik, Boltzmannstr. 2, DE-85748 Garching, Germany*
[6] *Department of Earth and Planetary Science, The University of Tokyo, Tokyo, 113-0033, Japan*

ABSTRACT

Collisionless shocks are common in astrophysical systems and stand as sites of particle acceleration. While particles at perpendicular shocks may not return to the upstream region, at oblique shocks a fraction of energetic electrons manage to escape the shock and travel upstream. An extended region known as the electron foreshock is formed, where these reflected particles drive various instabilities that may promote electron acceleration. Here we present the first 2D3V particle-in-cell (PIC) simulations of electron-ion non-relativistic oblique shocks that explore the interaction of the foreshock with pre-existing compressive turbulence with relative amplitude of 15% based on interstellar medium estimates. We find that pre-existing turbulence influences the emergence and behavior of the whistler-wave instability, as it enhances the amplitudes of the magnetic-field fluctuations and leads to larger nonlinear structures. This impacts the dynamics of the reflected electrons, resulting in a shorter and hotter electron foreshock. At the end of our simulations, with pre-existing upstream turbulence we observe non-thermal electrons that are more numerous, reach higher energies, and carry a larger portion of the total energy.

Keywords: acceleration of particles, instabilities, ISM – supernova remnants, methods – numerical, plasmas, shock waves

1. INTRODUCTION

Collisionless shocks are mediated by wave-particle interactions instead of binary Coulomb collisions and are known to produce relativistic particles. Diffusive shock acceleration (DSA; Axford et al. 1977; Krymskii 1977; Bell 1978; Blandford & Ostriker 1978) provides the basic description of particle acceleration, however it does not take into consideration pre-existing turbulence, which is a common feature in various astrophysical environments. Recent studies of weak heliospheric shocks (Guo et al. 2021; Perri et al. 2022; Trotta et al. 2021, 2023) and shocks propagating in relativistic pair plasma (Tomita et al. 2019; Demidem et al. 2023; Bresci et al. 2023) have shown that pre-existing turbulence does indeed play a significant role in the shock dynamics and particle acceleration.

In this work we focus on nonrelativistic high-Mach-number shocks with sonic and Alfvénic Mach numbers $M_s, M_A \gtrsim 20$, that are observed in supernova remnants (SNRs; see e.g., Reynolds 2008; Raymond et al. 2023) and in the solar system as the bow shocks of Jupiter (Slavin et al. 1985), Saturn (Sulaiman et al. 2015, 2016), and Uranus (Bagenal et al. 1987), and occasionally Earth (Sundberg et al. 2017; Madanian et al. 2021). SNRs are of our primary interest in this study, since they are persistent and resolvable sources that are widely accepted as plausible candidates for the production of galactic cosmic rays. When the supernova ejecta interacts with the ambient medium, strong shocks are formed. Their propagation velocities are typically in

Corresponding author: Karol Fulat
fulat@wisc.edu

the range of $v_{\rm sh} \approx 300 - 10,000$ km s^{-1} (Wang et al. 2009; Raymond et al. 2023). Synchrotron radiation produced by accelerated electrons explains radio observations (e.g., Shklovsky 1954; Dubner & Giacani 2015) and nonthermal X-ray emission (e.g., Koyama et al. 1995; Vink 2012). Moreover, γ rays emitted from these sources may have a leptonic origin, and be associated with energetic electrons (Pohl 1996; Brose et al. 2021).

DSA operates only with particles that are significantly more energetic than thermal particles. Thermal electrons, whose characteristic dynamical scales are much smaller than the shock width, cannot directly participate in DSA and must undergo pre-acceleration to reach the required energy threshold. This is known as the electron injection problem, which is a long-standing challenge in shock-acceleration physics (see, e.g., Amano et al. 2022; Bohdan 2023) and a relevant parameter for global models of cosmic-ray sources (see, e.g., Orlando et al. 2021, for a review).

Particle-in-cell (PIC) simulations describe collisionless plasmas from first principles and are therefore an excellent tool for investigating electron acceleration and nonlinear processes at electron kinetic scales. They are widely used to study particle acceleration in astrophysical plasmas (see Pohl et al. 2020, for a review), especially particle acceleration at SNR shocks (Bohdan 2023). In our previous work, we performed for the first time PIC simulations of nonrelativistic high-Mach-number shocks with a pre-existing turbulent upstream medium (Fulat et al. 2023). Our method of continuous turbulent plasma injection allows to perform simulations for previously unattainable spatial and temporal scales. The results indicated that at perpendicular shocks propagating in compressive turbulence, the behavior of electrons is not significantly different in comparison to the homogeneous upstream medium. Here, we study the shock-turbulence interplay at oblique nonrelativistic high-Mach-number shocks, where shock-reflected electrons drive various instabilities in the electron foreshock. For homogeneous upstream media Bohdan et al. (2022) found that in the outer foreshock region electrostatic electron-acoustic waves are present, while the inner foreshock is dominated by electromagnetic oblique whistler waves. The electron-acoustic waves carry less energy and can affect only less than 0.1% of the incoming electrons (Morris et al. 2022). The whistlers are gyroresonant with the shock-reflected electrons and have a significant effect on particle dynamics. In their 2D PIC simulations Morris et al. (2023) found a significant fraction of nonthermal electrons in the downstream energy spectrum, consistent with previous 1D simulations (Xu et al. 2020; Kumar & Reville 2021). Electrons are efficiently accelerated by a mechanism similar to stochastic shock drift acceleration (SSDA), for the first time observed in 3D shock simulations by Matsumoto et al. (2017) and described in detail by Katou & Amano (2019); Amano et al. (2022). Morris et al. (2023) observed more efficient acceleration than predicted by SSDA, possibly due to turbulent electric fields driven in the nonlinear regime of the whistler instability.

This paper explores the structure of oblique shocks, and the electron acceleration efficiency at them, for an upstream medium with pre-existing compressive turbulence. This paper begins with a description of the setup of simulations used in this study (Section 2) followed by a presentation of the results in Section 3. Finally, a summary and discussion are given in Section 4.

2. SIMULATION SETUP

In this work we use the fully relativistic PIC code THATMPI (Niemiec et al. 2008), which tracks two spatial and all three velocity components of the macroparticles describing the plasma (2D3V configuration). This setup optimizes computational resources and allows to run simulations with higher resolution compared to full 3D simulations while maintaining a reasonably accurate description of shock physics.

The simulation setup is similar to that of Fulat et al. (2023), in which we investigated perpendicular shocks with turbulent and homogeneous upstream media. Here, we briefly outline the setup and highlight differences. The shock wave in our simulation is established by reflecting a plasma beam off a conducting wall. The interaction between the incoming and the reflected beams then creates a shock. Since the simulation frame is equivalent to the downstream rest frame, the upstream plasma must be continuously replenished.

Whereas in previous simulations with a homogeneous upstream medium the upstream plasma was added in thin layers, plasma injection incorporating synthetic turbulence requires a new method Fulat et al. (2023). Prefabricated slabs of turbulent plasma are simulated in square boxes with periodic boundary conditions that are as wide as the main simulation box. Density fluctuations are established by initially imposing wave-like disturbances of the local bulk velocity. These slabs are then injected into the shock simulation, after matching them at the interface to prevent numerical transients. This matching technique provides a smooth transition of current densities and electromagnetic field between turbulent plasma over a selected region, which is obtained by interpolation of the field and the particle distribution function.

Table 1. Relevant plasma parameters for the initial setup of the simulations used in this study.

Parameter		Value
sonic Mach number	$M_{\rm s}$	36
Alfvénic Mach number	M_A	32
plasma beta	β_p	1
shock speed	$v_{\rm sh}$	$0.264c$
electron thermal velocity	$v_{{\rm th},e}$	$0.057c$
number of particles per cell	n_0	20
electron skin depth	$\lambda_{\rm se}$	20Δ
mass ratio	m_i/m_e	100
turbulence level	$\delta n/n$	15% (run T) - (run H)

Here, Δ represents the computational cell size, and c denotes the speed of light. Refer to the main text for definitions of all parameters.

Oblique-shock simulations require extended boxes in order to contain the electron foreshock. For pre-existing turbulence injected at the outer right boundary, advection towards the shock takes longer than in perpendicular-shock simulations. Therefore, the turbulence decay time must be increased, which motivates the use of larger simulation boxes than in our previous study, $L_y \approx 12\lambda_{\rm si}$ instead of $L_y = 6\lambda_{\rm si}$. A secondary benefit of this choice is that nonlinear structures driven by the whistler instability with sizes up to $5\lambda_{\rm si}$ can be fully captured (see Morris et al. 2023).

We performed two simulations, one with density fluctuations of amplitude $\delta n\,/n_0 = 15\%$ (run T) and one with a homogeneous upstream medium (run H). The fluctuation amplitude, δn, is calculated as the root mean square (rms) of the particle density measured in small tiles that are a quarter of ion skin length in size, and n_0 is the mean density. The magnitude of the density fluctuations on kinetic scales for SNRs are unknown. In the simulation, larger fluctuation levels would lead to strong heating that compromises the sonic Mach number. Our choice of amplitude avoids that and corresponds to measurements in the heliosphere (Carbone et al. 2021) and the local interstellar medium (Lee & Lee 2020; Ocker et al. 2021; Fraternale et al. 2022), which show $\delta n\,/n_0 \lesssim 10\%$.

Table 1 shows the relevant plasma parameters for each simulation. The initial large-scale magnetic field has an out-of-plane configuration, $\mathbf{B}_0 = B_0(\cos\theta_0, 0, \sin\theta_0)$, where the obliquity angle is $\theta_0 = 60°$. This choice provides the same number of degrees of freedom and adiabatic index of plasma as a 3D setup. It was also used in Morris et al. (2023), since it fully captures the oblique whistler waves.

We initialize the upstream plasma with twenty particles per cell for both ions and electrons, $n_0 = n_i = n_e = 20$, where the subscripts "i" and "e" represent ions and electrons respectively. The plasma flows toward the reflecting wall with velocity $\mathbf{v_0} = v_0\hat{x}$, where $v_0 = -0.2c$ and c is the speed of light. The expected shock speed in the upstream frame is $v_{\rm sh} \simeq 0.264c$.

In the shock simulation the particles are initially in thermal equilibrium at $T_e \approx T_i \approx 1.6 \cdot 10^{-3} m_e c^2/k_B \approx 1.6 \cdot 10^{-5} m_i c^2/k_B \approx 10^7$ K, where T are temperatures, m particle masses, and k_B is the Boltzmann constant. For such non-relativistic conditions the thermal speed of electrons is $v_{th,e} = \sqrt{2k_B T_e/m_e} \simeq 0.057c$, and ten times smaller for ions, on account of the ion-to-electron mass ratio $m_i/m_e = 100$. The plasma beta, defined as the ratio of the thermal pressure to the magnetic pressure, is $\beta_p \approx 1$ for all runs. The sonic Mach number then follows as $M_{\rm s} = v_{\rm sh}/c_S \approx 36$ for all runs, where $c_S = \sqrt{\Gamma k_B (T_e + T_i)/m_i} \approx 0.0074c$, where c_S is the sound speed and $\Gamma = 5/3$ is the adiabatic index. Likewise, the Alfvén speed $v_A = B_0 c/\sqrt{n_0(m_e + m_i)} = 0.00829c$ leads to an Alfvénic Mach number $M_A \approx 32$. The expected compression ratio at the shock is $r \simeq 3.97$.

The time step, $\delta t = 1/40\,\omega_{pe}^{-1}$, scales with the electron plasma frequency, $\omega_{pe} = \sqrt{e^2 n_e/(\epsilon_0 m_e)}$, where e is the elementary charge and ϵ_0 is the vacuum permittivity. We evolve the system for approximately $20\,\Omega_i^{-1}$ in ion cyclotron times, $\Omega_i^{-1} = m_i/(eB_0) \approx 48,000\delta t$. The electron skin depth is $\lambda_{\rm se} = c/\omega_{pe} = 20\Delta$, where Δ represents the cell size; for ions it is higher by a factor $\sqrt{m_i/m_e} = 10$.

Our choice of simulation parameters is a compromise between computational expedience and the accurate modeling of the shocks. By using a shock speed that is higher than that typically found in SNRs, but still nonrelativistic, we are able to extend the duration of our simulations. In addition, these parameter choices allow for a direct comparison with previous studies of high-Mach-number shocks.

3. RESULTS

In this section, we compare the results of simulations with an initially turbulent (run T) and a homogeneous (run H) upstream medium. Our focus is on the influence of pre-existing turbulence on the global shock structure, the shock velocity, magnetic-field amplification, and the properties of the nonlinear structures developed by the oblique whistler instability. We then investigate how the plasma waves are affected by the pre-existing tur-

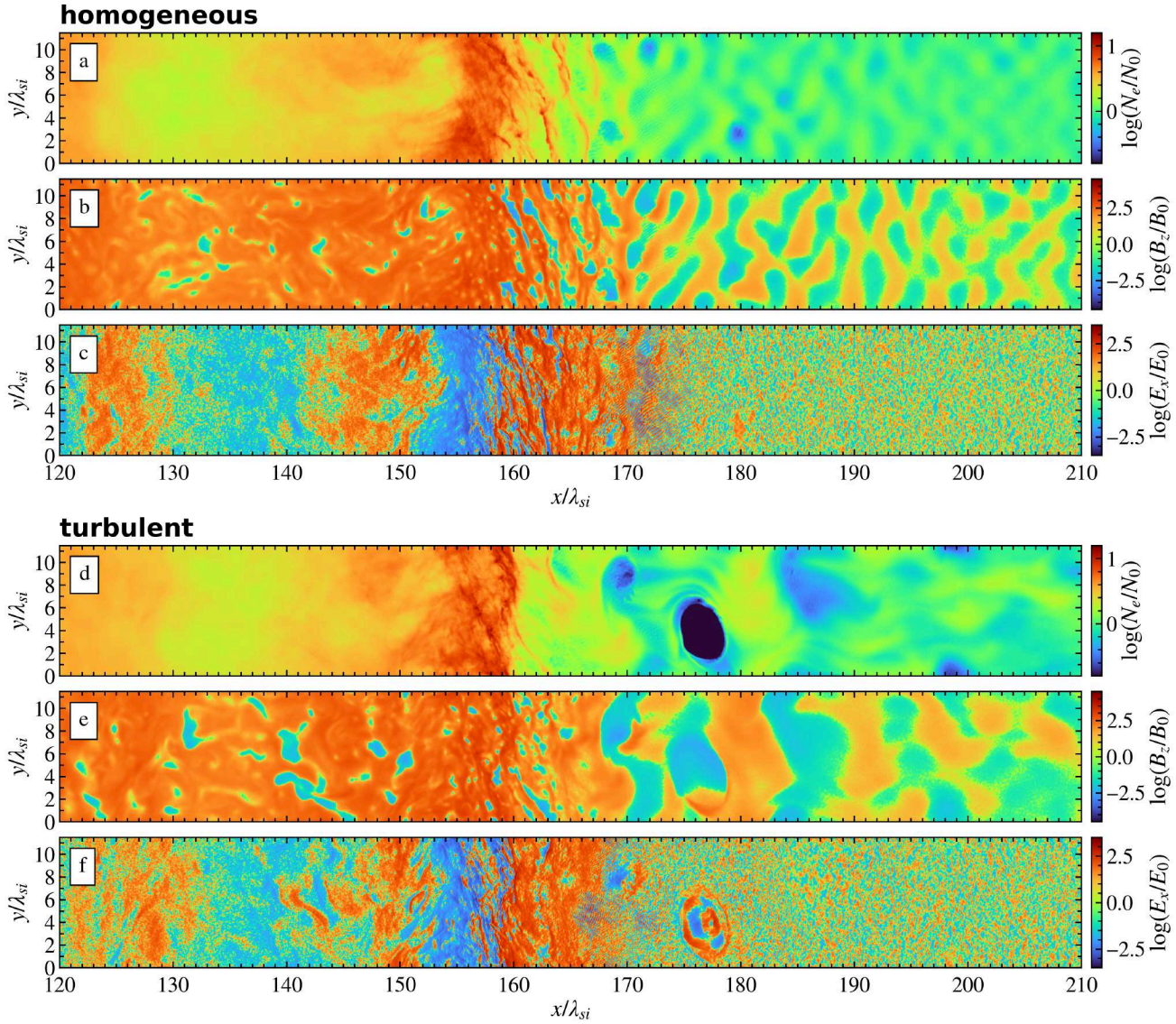


Figure 1. Maps of the electron number density (panels a and d), the z-component of the magnetic (panels b and e), and the x-component of electric fields (panels c and f) at an oblique shock with pre-existing upstream density fluctuations (run T, panels d,e, and f) and with a homogeneous upstream medium (run H, panels a,b, and c), both at $t \approx 18\,\Omega_i^{-1}$. For the B_z map, the initial upstream field was subtracted. The scaling of the fields is logarithmic and sign preserving, e.g., for B_x/B_0 it is $\mathrm{sgn}(B_x) \cdot [2 + \log\{\max(10^{-2}, |B_x|/B_0)\}]$.

bulence. Moreover, we examine the influence of the turbulence on the shock-reflected electron distribution. Finally, we study the electron energy spectra in the downstream region.

3.1. *Global shock structure*

Generally, shock-reflected ions determine the structure of supercritical shocks. However, at oblique shocks, a significant portion of the reflected particles are electrons. They form a complex structure known as the electron foreshock. Of the two main instabilities driven there, the electron-acoustic waves are expected to be weak for the out-of-plane configuration of our simulation (Bohdan et al. (2022), Morris et al. (2022)), and they are not considered in the present analysis. After a few ion Larmor times, the electromagnetic oblique-whistler instability driven in the inner foreshock develops into its nonlinear stage and creates wavepackets that are advected with the incoming flow. They interact with the shock and modify the shock foot and ramp.

Figure 1 compares the electron number density, the z-component of the magnetic field, and the x-component of the electric field at a late stage of the two simulations, at $t \approx 18\,\Omega_i^{-1}$. The plot covers only the inner part of the electron foreshock, where the whistler waves are present. Panels (a) and (d) of Figure 1 show that

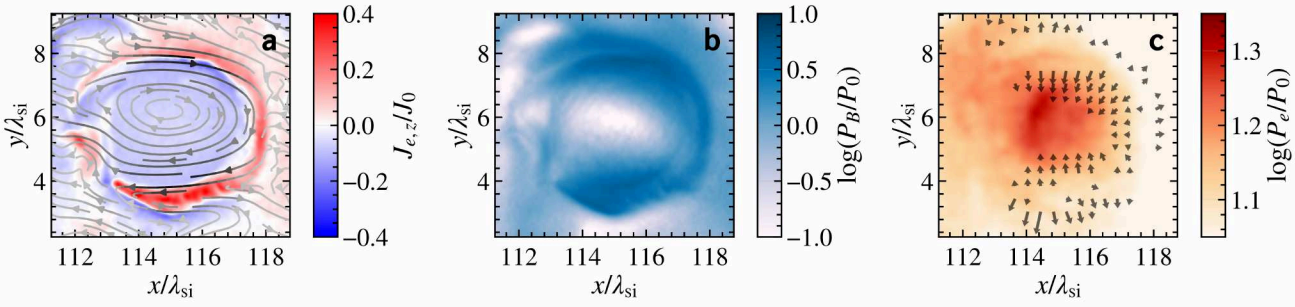


Figure 2. Structure of an example nonlinear cavity observed in the foreshock of the turbulent simulation. Panel a shows the J_z component of the electron current density normalized to $J_0 = q_e n_0 v_0$ with superimposed magnetic-field lines, their colour-shade representing their strength. Panels b and c show the magnetic and electron pressures, respectively, that are normalized by the initial pressure, $P_0 = B_0^2/2\mu_0 + n_0 k_B(T_e + T_i)$. Arrows on panel c represent the $\mathbf{J} \times \mathbf{B}$ force field.

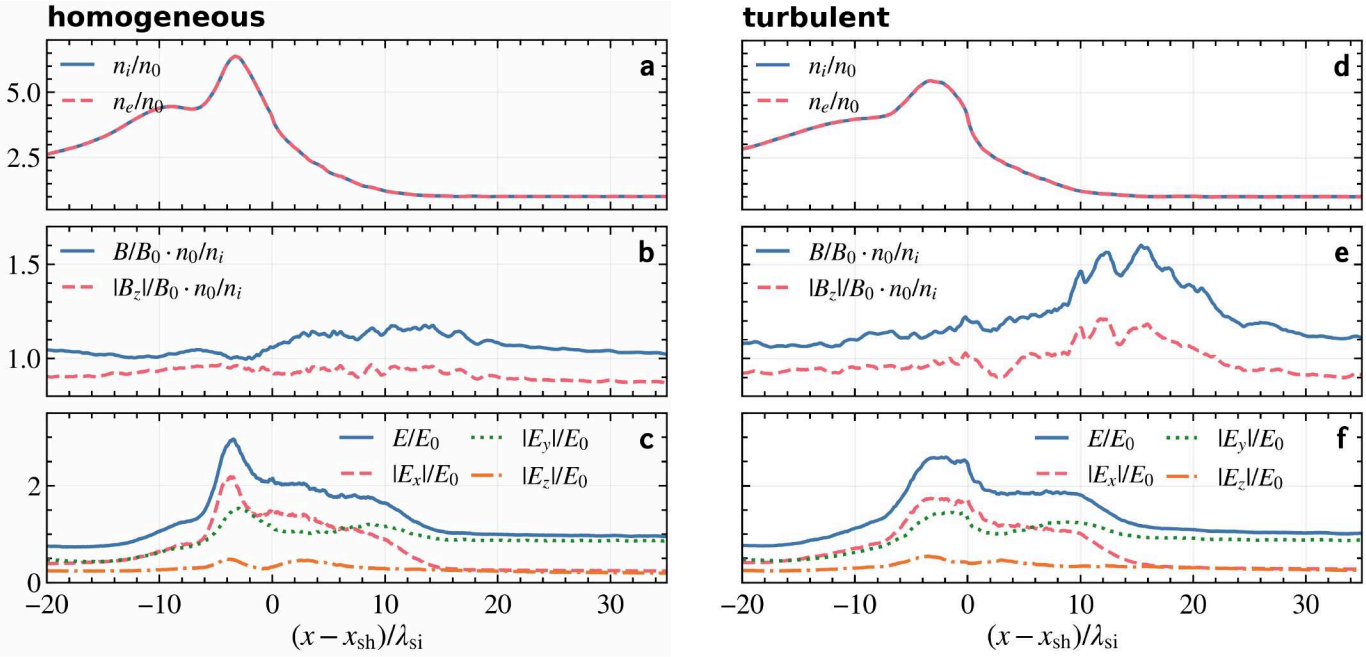


Figure 3. The ion and electron number density profile (panels a,d), the ratio of the magnetic field strength to the density (panels b,e), and the electric field profiles (panels c,f) averaged over the y-direction, for run H (panels a,b, and c) and T (panels d,e, and f). The profiles are time-averaged from $t\Omega_i \approx 7$ to $t\Omega_i \approx 20$.

these waves are stronger closer to the shock front since the energy density of the reflected electrons decreases with distance from the shock. The nonlinear structures developed by the instability, such as cavities with bipolar magnetic-field features, appear at about $t \approx 9\Omega_i^{-1}$ for the homogeneous simulation and at about $t \approx 7\Omega_i^{-1}$ in the presence of pre-existing turbulence. For the initially turbulent upstream medium in run T they can be as large as $7\lambda_{si}$, to be compared to roughly $2\lambda_{si}$ for run H.

Figure 2 shows the structure of a representative cavity from the turbulent simulation, with all quantities computed in the upstream rest frame. Since the bipolar magnetic field has mostly in-plane components, the magnetic-field lines depicted in panel (a) thus give a fair impression of the full magnetic-field structure. This field is generated by the J_z component of the electron current density. The negative J_z current derives from the drift of reflected electrons along the background magnetic field which is only 30° off the z axis. The lighter color of the streamlines in panel (a) indicates that the magnetic field strength decreases towards the cavity center. This is also apparent in panel (b), which presents the magnetic pressure. Panel (c) illustrates a high electron pressure inside the structure, where the hot, low-

density reflected electrons are accumulated[1]. The corresponding outward-directed force is compensated by the Lorentz force on these particles that tends to confine them inside the structures (Morris et al. 2023), which is indicated by the arrows in this panel. At the cavity boundary, the Lorentz force pushes the dense and cold background particles outward.

The average perpendicular electron momentum inside the cavity is approximately $p_\perp/m_e c \approx 4$. With the magnetic field roughly twice the background value, the gyroradius is $r_g \approx 2\lambda_{\rm si}$, comparable to the structure radius $R \approx 2\lambda_{\rm si}$. The electrons inside the cavity have a non-zero velocity in the x-direction, $v_x \approx 0.4c$, and so their cavity-crossing time is $\tau = 2R/v_x \approx 10/\omega_{pi}$. This is larger than the reciprocal of the electron gyrofrequency, $\gamma_{\rm e}\Omega_{\rm e}^{-1} \approx 2.5/\omega_{pi}$, for the typical Lorentz factor $\gamma_{\rm e} \approx 4$. Therefore, shock-reflected electrons of moderate energy are likely confined within, which is consistent with previous studies (see Section 4.5 in Morris et al. 2023). The balance of the magnetic and electron pressures causes these structures to inflate as they are advected towards the shock. Ion pressure is omitted from the discussion, as this species exhibits no distinct pressure signatures in these cavities. The properties of the cavities observed in the homogeneous simulation are analogous, although their scale is smaller and their electron pressure is lower.

In Figure 1 the shock foot is located between $x = 170\lambda_{\rm si}$ and $x = 175\lambda_{\rm si}$. In its vicinity, the Buneman instability drives strong electrostatic modes which are visible as striped motifs in the E_x maps. Hereafter, we use them as an indicator of the shock position. We note that the cavities in Figure 2 emerge beyond the shock foot in the foreshock region. The shock ramp contains the characteristic filaments of the Weibel instability that is driven by counter-streaming ions. It is strongest for wavevectors perpendicular to the relative velocity between the shock-reflected and incoming ions. The filaments are oblique because the bulk-gyrating ions have a non-zero v_y velocity component. The transition to the downstream region is marked by the overshoot-undershoot pattern that extends over roughly 5-10$\lambda_{\rm si}$ behind the shock front.

Figure 3 shows profiles averaged over the y-direction of the ion number density and the absolute strength of the magnetic and electric fields. The profiles are time-averaged, starting from the beginning of the regular shock reformation at $t\Omega_i \approx 7$, up until the end of the simulation, (see the top panel in Figure 4 and the subsequent paragraph for further details). Comparing the density profiles for runs H and T, shown in panels (a) and (d), reveals that with pre-existing turbulence the overshoot is wider in size and the undershoot is less pronounced. The compression ratio is consistent with an MHD shock expectation for both simulations. As previously mentioned, the out-of-plane configuration of the external magnetic field weakens the presence of the Weibel instability. Therefore, the growth of the magnetic field in the shock transition region is primarily due to the compression of the B_z component of the initial magnetic field $\mathbf{B_0}$, as $|B_z|/n_i$ is nearly constant. In both runs, the main amplification of the magnetic field begins at about $30\lambda_{\rm si}$ ahead of the shock front (Figure 3b,e) which corresponds to the region where the nonlinear structures develop. For the run with the pre-existing density fluctuations, the magnetic field in the corresponding region is stronger by approximately 25%. The constant E_y component of the electric field in the upstream region is the motional electric field, $\mathbf{E}_0 = -\mathbf{v}_0 \times \mathbf{B}_0$. In the shock foot region, the Buneman instability enhances E_x and E_y, as the wavevectors lie in the x-y plane. In the ramp region, a charge-separation field is present, indicated by the increase of the E_x in Figure 3c,f. Both E_x and E_y are amplified in the overshoot region. Though poorly observable, the magnitude of E_z is also enhanced. Strong electric fields at the shock ramp are paramount for efficient electron acceleration. Morris et al. (2023) report that the energy gain of electrons at the shock is much larger than the work done by drifting along the motional electric field, with E_x and E_z significantly contributing. This leads to a more efficient acceleration than typically expected from SSDA.

Figure 4 shows the evolution of the y-averaged electron density for simulations with homogeneous (run H, top panel) and turbulent upstream plasma (run T, bottom panel). Following a swing-in phase that lasts about $t \approx 7\Omega_i^{-1}$, cyclic shock reformation is visible as modulations of the shock front in run H. The reformation period is, on average, roughly $1.6\Omega_i^{-1}$, which is consistent with the results for perpendicular shocks, except for the delayed appearance (see, e.g., Wieland et al. 2016; Bohdan et al. 2017; Fulat et al. 2023). The dark blue stripes located ahead of the shock front in the top panel represent the whistler-driven structures. They become evident at about $t \approx 7 - 9\Omega_i^{-1}$, reflecting the nonlinear stage of the whistler instability. In the bottom panel of Figure 4 representing run T, the x-t traces of the pre-existing density fluctuations are visible as straight features at all times. The amplitude of the upstream perturbation increases with time, and the features develop sub-structure, suggesting that, when the upstream

[1] This is verified by comparing the electron momentum distributions inside the cavity and at its boundary.

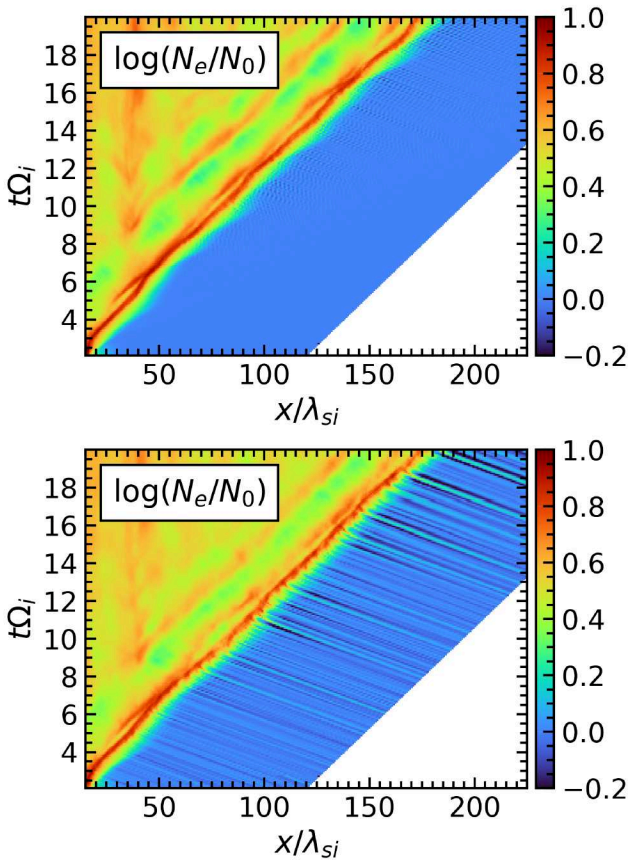


Figure 4. Evolution of the ion number density averaged over the y-direction for run H (top panel) and T (bottom panel). For visualization purposes, the presentation is truncated $110\lambda_{\rm si}$ ahead of the shock.

medium is initially turbulent, the nonlinear structures develop earlier, are stronger, and/or appear more frequently. Shock-front corrugation is superimposed on the reformation pattern for run T. The structure of the overshoot is blurred, and the peak density is slightly lower than for homogeneous conditions.

3.2. *Wave modes in the foreshock region*

Previous shock simulations with a homogeneous upstream medium demonstrated that, for out-of-plane magnetic-field configurations, oblique whistler waves are the dominant modes in the inner foreshock region (Morris et al. 2023). With a few ion skin lengths (see Fig.7 of Bohdan et al. 2022), their wavelengths are comparable to the characteristic length scales of the pre-existing turbulence in run H. Consequently, it is challenging to distinguish the modes in the power spectrum of magnetic-field fluctuations. Instead, the right-hand circular polarization of the whistler waves can be used for identification.

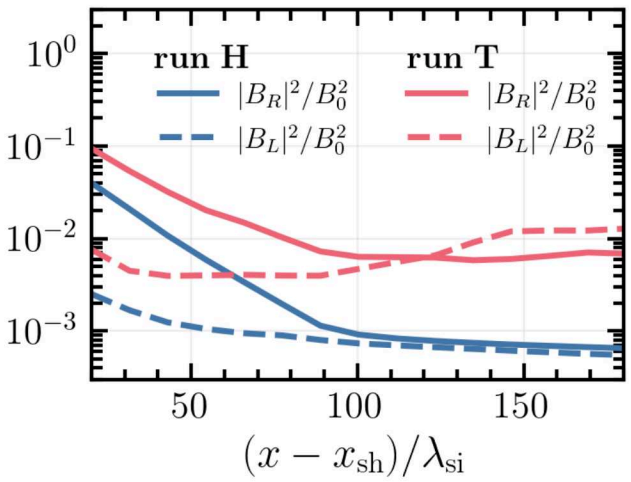


Figure 5. The energy density of the right (solid lines) and left (dashed lines) circularly polarized modes in the foreshock region for run H (blue lines) and run T (red lines). The energy density is normalized to the energy density of the initial magnetic field.

In our simulations, the wavevector of a whistler wave must lie in the x-y plane, $\mathbf{k} = (k_x, k_y)$. Defining $\theta(\mathbf{k}) \equiv \angle(\mathbf{k}, \hat{\mathbf{x}}) = \arctan(k_y/k_x)$, the Fourier amplitudes of waves for right-hand circular (subscript R) or left-hand circular (subscript L) polarization, B_R and B_L, can be written as

$$\widetilde{B_R}(\mathbf{k}) = \widetilde{B_z}(\mathbf{k}) - i\sin[\theta(\mathbf{k})]\widetilde{B_x}(\mathbf{k}) + i\cos[\theta(\mathbf{k})]\widetilde{B_y}(\mathbf{k}), \quad (1)$$

$$\widetilde{B_L}(\mathbf{k}) = \widetilde{B_z}(\mathbf{k}) + i\sin[\theta(\mathbf{k})]\widetilde{B_x}(\mathbf{k}) - i\cos[\theta(\mathbf{k})]\widetilde{B_y}(\mathbf{k}), \quad (2)$$

where the tilde represents the transform. A derivation of this expression can be found in Appendix A. These quantities are calculated in the upstream reference frame to preserve the intrinsic polarization pattern of the waves. Calculating the absolute values yields power spectra characteristic of right-hand and left-hand circularly polarized modes, and Parseval's theorem directly provides the energy density of the magnetic field associated with the modes.

Figure 5 shows the energy density of modes with right or left-hand circular polarization in the inner foreshock region for both simulations. The energy densities at a given location are determined from the power spectra of B_R and B_L calculated within a square region of size: $x \in [x - L_y/2, x + L_y/2], y \in [0, L_y]$, time-averaged over the reformation cycle that follows the emergence of the nonlinear structures in the homogeneous simulation, $11 \lesssim \Omega_i t \lesssim 12.5$, and normalized to the energy density of the background magnetic field. With a homogeneous

upstream medium (run H), B_R and B_L have small amplitudes at distances $x - x_{\rm sh} \gtrsim 90\lambda_{\rm si}$, indicating that there are no strong electromagnetic waves this far upstream. In the range $20\lambda_{\rm si} \lesssim x - x_{\rm sh} \lesssim 90\lambda_{\rm si}$, the magnitude of B_R grows exponentially, indicating the driving of right-hand polarized waves. At $x - x_{\rm sh} \approx 20$ the nonlinear structures start to emerge.

Due to their relatively low phase and group velocities, whistler waves comove with the background plasma. Consequently, the spatial amplification of their amplitudes along the x-direction is equivalent to temporal growth, as $(x - x_{\rm sh}) = C - v_{\rm sh}t$. The exponential slope in Figure 5 hence is a measure of the growth rate of the right-hand polarized mode, γ, as

$$|B_R|^2 \propto \exp\left(-2\gamma \frac{x - x_{\rm sh}}{v_{\rm sh}}\right). \quad (3)$$

The fitted growth rate equals $\gamma_{\rm H} = (8.16 \pm 0.33) \times 10^{-3}\Omega_e$ for the homogeneous run, where the uncertainty range is for 95% confidence level (2σ). Bohdan et al. (2022) conducted periodic-box simulations with particle distributions close to those in the electron foreshock of our shock simulations, and they found consistent agreement with the results yielded by linear analysis of oblique whistler waves.

For run T, the energy densities for the two polarizations are comparable in the far-upstream region and reflect the properties of the pre-defined compressive turbulence (see Appendix B for further details). As in the homogeneous simulation, at around $x - x_{\rm sh} \approx 90\lambda_{\rm si}$, B_R starts to grow exponentially toward the shock front. An exponential-function fit yields a growth rate of $\gamma_{\rm T} = (5.8 \pm 0.58) \times 10^{-3}\Omega_e$, which is lower than that derived from run H. This may be a consequence of the higher temperature of the shock-reflected electrons with preexisting turbulence (see Section 3.3), that leads to lower growth rates (see Figure 11 in Bohdan et al. 2022).

The amplitude of the whistler waves at $x - x_{\rm sh} \approx 20\lambda_{\rm si}$ remains constant for the duration of our simulations, $|B_R|^2/B_0^2 \simeq 0.04$ and $|B_R|^2/B_0^2 \simeq 0.1$, but in both runs the wave growth begins at progressively larger distances from the shock.

3.3. *Electron foreshock properties*

Figure 6 compares the electron phase-space distributions for runs H and T at the end of the simulations (at about 20 ion Larmor times), when the shock front is located at $x_{\rm sh} \approx 177\lambda_{\rm si}$. Ahead of the shock, the cold incoming particles are represented by a narrow strip centered around $(p_x, p_y, p_z)/mc = (-0.2, 0, 0)$. The other particles present at $x \gtrsim x_{\rm sh}$ are the shock-reflected electrons.

When the upstream medium is initially homogeneous (panels a,b, and c), the electron foreshock extends up to $670\lambda_{\rm si}$. The momentum spread of the shock-reflected electrons decreases with distance from the shock, and so does the amplitude of the whistler waves with which the electrons are gyroresonant, suggesting a declining scattering efficiency (see Section 3.2). In contrast, for turbulent upstream conditions, run T (panels d, e, and f), the electrons do not travel that far, and the right boundary of the foreshock lies at $540\lambda_{\rm si}$, closer to the shock by 25% or roughly five Larmor radii of the upstream ions. Also, the distribution of the reflected electrons appears wider, hence hotter, suggesting enhanced scattering in the foreshock.

To study the properties of shock-reflected electrons in greater detail, we separate them from the incoming electron beam. We compute the three-dimensional momentum distributions of electrons in the upstream rest frame within regions of $50\lambda_{\rm si}$ width and height L_y, choosing a coordinate system in which one axis is aligned with the initial magnetic field. Then, we fit a drifting nonrelativistic Maxwellian to these distributions, assuming it represents the background (incoming) electrons. We obtain the reflected electron distribution by excluding particles within a sphere centered on the average background electron momentum with a radius of three times the rms momentum of background electrons. The particle count inside this sphere is subsequently interpolated. After accounting for uncertainties due to particle statistics and binning procedures, we estimate the uncertainty in both the average and the rms momenta of the background and shock-reflected electrons to be $10^{-3}m_ec$ and $10^{-4}m_ec$, respectively.

Figure 7 compares the parallel component of the average momentum, $p_{\rm av,\parallel}$, between the homogeneous and turbulent simulations. In the far-upstream region at$x \approx 600\lambda_{\rm si}$, the parallel momentum is approximately zero for both cases, as expected. Approaching the shock front, it becomes negative, indicating that a return current is established that neutralizes the current of the shock-reflected electrons. The parallel momentum plateaus at around $x \lesssim 400\lambda_{\rm si}$ for run H and at $x \lesssim 300\lambda_{\rm si}$ for run T.

Figure 8 presents the number density (panel a), the parallel component of the average momentum (panel b), the perpendicular component of the rms momentum (panel c), and the kinetic-energy density of the reflected electrons. The rate at which the number density increases from the upstream region to the shock front (right to left) is similar for the homogeneous and turbulent simulations, but, due to the shorter foreshock in run T, the red dashed line is shifted left by roughly

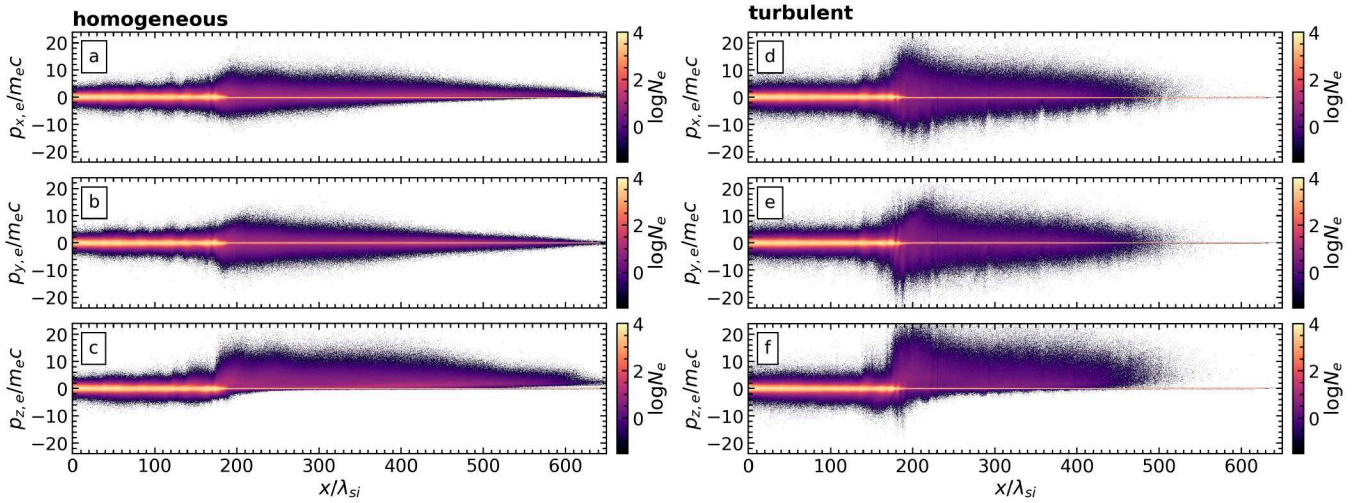


Figure 6. Electron phase-space distributions for run H (panels a,b, and c) and run T panels (d,e, and f) at time $t \approx 20\Omega_i^{-1}$.

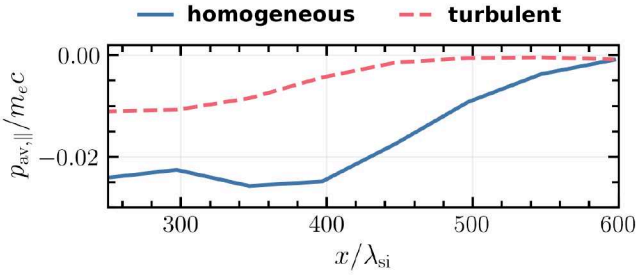


Figure 7. The parallel component of the average momentum of the background electrons in the upstream rest frame.

$x \approx 100\lambda_{\mathrm{si}}$, translating to a lower density at a given location. A similar trend is seen in panel b) of the figure. Panel c illustrates that the rms momentum, $p_{\mathrm{rms},\perp}$, is significantly larger with pre-existing turbulence. As the $p_\perp$ component is Lorentz-invariant, its rms value reflects the perpendicular temperature of the beam of reflected electrons that is higher in the turbulent simulation, at least for a large part of the foreshock. The energy density of the reflected electrons within $x \approx 100\lambda_{\mathrm{si}}$ of the shock front is comparable in both simulations, and further out there is much more energy density in the foreshock for homogeneous initial conditions (Panel d).

3.4. *Electron acceleration*

Figure 9 shows the electron energy distribution in the downstream region for the simulations H and T. The spectra are computed in the local plasma rest frame in the region between $20\lambda_{\mathrm{si}}$ and $90\lambda_{\mathrm{si}}$ behind the shock at the final time step of our simulations, $t \approx 20\Omega_i^{-1}$. Low-energy electrons are well represented by a relativistic Maxwellian distribution. As expected from previous studies, both simulations demonstrate a nonthermal spectral tail of the form $N(\gamma) \propto (\gamma - 1)^s$ that extends

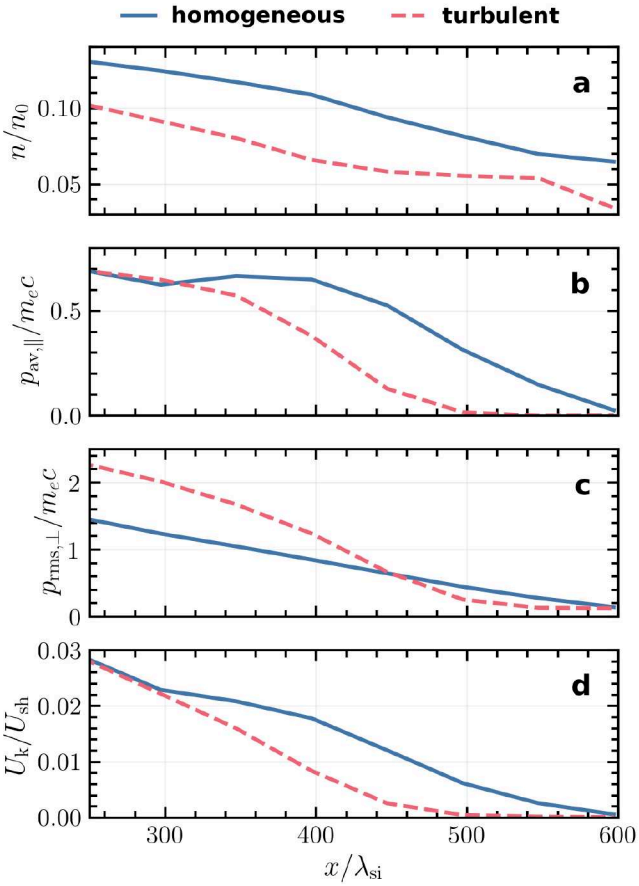


Figure 8. The number density (panel a), the parallel component of the average momentum (panel b), the perpendicular component of the rms momentum (panel c), and the energy density (panel d) of the shock-reflected electrons. All quantities are calculated in the upstream rest frame.

to higher energies for run T. In the homogeneous simulation, the fraction of non-thermal electrons, defined

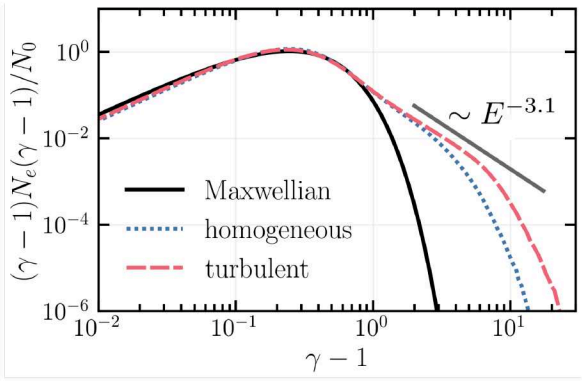


Figure 9. The electron energy spectrum in the downstream regions for runs T (turbulent; the red-dashed line) and H (homogeneous; the blue-dotted line). The black solid line denotes a fitted relativistic Maxwellian to the low-energy part of the distribution. The grey solid line represents the slope of the nonthermal tail.

as particles with $\gamma - 1 \geq 3$, is approximately equal to 0.14%. These particles account for about 1.9% of the total electron energy. For the simulation with pre-existing turbulence, these values are 0.23% and 3.6%, respectively, and the maximum Lorentz factor is 40% higher than without pre-existing turbulence.

4. SUMMARY

We have performed 2D3V PIC simulations of nonrelativistic oblique shocks propagating in an electron-ion plasma with pre-existing density fluctuations of amplitude 15%. The physical parameters are chosen to model conditions in SNRs, and so the shocks have high Mach numbers and propagate in a medium with a plasma beta near unity. Our main objective was to investigate the influence of turbulence on the foreshock properties, the whistler instability, and electron acceleration. The fluctuation level, $\delta n/n = 15\%$, is chosen to avoid excessive heating and is consistent with in-situ measurements of density fluctuations of the local interstellar medium. We used a sufficiently large simulation box in the transverse direction to capture large nonlinear structures driven by the electromagnetic whistler instability. We directly compared the turbulence's influence on shock properties and electron acceleration to a simulation with a homogeneous upstream medium. Furthermore, we examined the global shock structure along with the magnetic-field amplification. Our key conclusions are:

1. The shock structure is slightly modified by the pre-existing turbulence; the overshoot is wider, and the undershoot is less pronounced. In the out-of-plane configuration that we employed, the Weibel instability in the shock ramp is weakened, and so the magnetic field is amplified only by whistler waves ahead of the shock front. We measure amplitudes of the magnetic field about 25% higher for the simulation with pre-existing turbulence in this region.

2. A return current is established by background plasma that neutralizes the current of the shock-reflected electrons. This current is caused by background electrons that gradually accelerate as they approach the shock front.

3. Our simulations indicate that pre-existing density fluctuations cause the length of the electron foreshock to decrease by approximately ~ 5 ion gyroradii. Furthermore, the shock-reflected electrons have a higher temperature.

4. Both simulations show modes with right circular polarization in the upstream rest frame, within the foreshock region. The growth rates are comparable to the peak growth rate of the oblique whistler instability (for similar plasma parameters). Therefore, we conclude that the observed modes are oblique whistler waves.

5. The growth rate of the whistler waves is lower by roughly one third in the presence of pre-existing density fluctuations. This is likely due to larger temperature of the shock-reflected electrons, or smaller temperature anisotropy of the beam. For both simulations, the growth rates decrease with time, but the whistler waves start to grow at larger distances from the shock, and their amplitude near it remains the same.

6. Nonlinear structures similar to those driven by whistlers at the homogeneous shock appear two ion cyclotron times earlier for a run with turbulence, and their maximum size is larger: $7\lambda_{si}$ compared to $3\lambda_{si}$.

7. The nonlinear structures feature high electron pressure due to the confinement of the shock-reflected electrons. This leads to pressure imbalance between the interior and exterior of these structures, causing them to expand as they propagate towards the shock front. Since the nonlinear structures are larger in size and have stronger electromagnetic fields, they eventually distort the shock front to a greater extent when they merge with it.

8. The high-energy tail of the downstream electron spectrum is well described by $N(\gamma) \propto (\gamma - 1)^{-3.1}$ in both cases, but electrons are accelerated more

efficiently in the presence of pre-existing turbulence, as both their number (0.23% vs 0.14% of total electrons present in the downstream region) at the end of the simulation) and energy (3.6% vs 1.9%) densities are higher than for a homogeneous upstream medium. Likewise, the maximum electron energy is higher by 40%.

The simulations presented in this study are of higher resolution but have shorter duration ($t\Omega_i \approx 20$ vs. $t\Omega_i \approx 50$) than previous 2D3V PIC simulations of high-Mach-number oblique shock that also employed different electron-ion mass ratios (Bohdan et al. 2022; Morris et al. 2023). The previous studies showed that after approximately 30 ion Larmor times the nonlinear cavities reached a size of a few ion skin lengths. In the run with pre-existing turbulence we observe that the nonlinear structures are larger and appear earlier. But the final size of these structures remains uncertain, and they may eventually reach a similar size with and without pre-existing turbulence that may be related to scales of the whistlers at their saturation, the characteristic scales of the pre-existing turbulence, or the simulation-box size.

The linear growth of the electron whistler instability is independent of the ion-to-electron mass ratio, but the spatial size of the region where the whistler growth is observed decreases (in ion scales) as the mass ratio increases. The argument of the exponential in Equation 3 can be written as $-2(\gamma/\Omega_e)\cdot M_A^{-1}\cdot m_i/m_e\cdot(x-x_{\rm sh})/\lambda_{\rm si}$. For the same magnetic-fluctuation amplitude near the shock front, growth rate, and Alfveńic Mach number, the spatial size of the whistler growth region scales inversely with the mass ratio. As $M_A\lambda_{\rm si}$ is the ion gyroradius for the shock speed, which is a proxy of the shock thickness, for a realistic m_i/m_e the spatial scale of wave growth becomes comparable to the shock thickness. It is unclear whether that leads to larger wave amplitudes or to faster return of reflected electrons to the shock, but in any case we expect an impact on the electron acceleration efficiency.

The nonlinear cavities in our simulations exhibit similarities with microscale coherent structures that are commonly observed in turbulent plasmas throughout the heliosphere. High-resolution observations from the Magnetospheric Multiscale (MMS) mission identified kinetic-scale magnetic holes in the Earth's magnetosheath, ranging in size from one ion gyroradius to a few electron gyroradii (see, e.g., Shi et al. 2024, for a review). These structures feature a magnetic field depression, typically accompanied by an increase in the particle density and temperature. One of their possible generation mechanisms is associated with electron temperature anisotropy regions in plasma turbulence that are unstable to oblique electron whistlers that convert to Bernstein modes and then collapse (Espinoza-Troni et al. 2025). In simulations of decaying turbulence, they seem to emerge from electron velocity shear (Arrò et al. 2023). Earth's foreshock transients are phenomena showing a decrease in the magnetic field. Some of them, such as hot flow anomalies, spontaneous hot flow anomalies, and density holes, are associated with depletions in the number density and particle heating in the core, as well as compressions at the edges (see, e.g., Zhang & Zong 2020; Zhang et al. 2022). The beam of reflected electrons in our simulations provides substantially different initial conditions than those found in the turbulent plasma of the solar wind or magnetosheath plasma (for example fast relative streaming of two populations of electrons rather than a temperature anisotropy). The fact that the structures we see are not identical yet share similitude with those in heliosphere suggests that such solitary structures are produced in a variety of environments and for range of conditions.

Currently, fully kinetic 3D simulations are overwhelmingly challenging. They are limited to lower resolutions and smaller box sizes, and they reach the earliest stages of the system's evolution when the electron foreshock has not yet formed (Matsumoto et al. 2017). Orusa & Valenzuela-Villaseca (2025) argue that for our choice of parameters 2D simulation should provide a reasonable description of ion acceleration, but including all dimensions may affect the interplay and nonlinear development of electron acceleration and instabilities driven at the shock. For example, in the out-of-plane configuration used in this work, the Weibel instability is suppressed, so the interplay between pre-existing modes, whistlers, and the Weibel instability should be investigated in three spatial dimensions.

The level of pre-existing compressible turbulence that can be achieved on kinetic scales is limited by particle heating. To maintain sufficiently strong sonic Mach numbers, $M_s \gtrsim 30$, the maximum level of the density fluctuations should be on the order of $\delta n/n \sim 15\%$, with a few times lower amplitudes of the magnetic field fluctuations (Fulat et al. 2023). Future studies will explore the effect of Alfveńic turbulence, in which the magnetic-field fluctuations dominate and may reach higher amplitudes without excessive heating.

K.F. acknowledges support by the Simons Foundation as part of Simons Collaboration on Extreme Electrodynamics of Compact Sources (SCEECS). E.M. and M.P. acknowledge support by DFG through grant PO 1508/11-1. This research was supported by the International Space Science Institute (ISSI) in Bern, through ISSI International Team project #520 *Energy Partition across collisionless shocks* and by the Munich Institute for Astro-, Particle and BioPhysics (MIAPbP), which is funded by the Deutsche Forschungsgemeinschaft (DFG, German Research Foundation) under Germany´s Excellence Strategy – EXC-2094 – 390783311. M.T. acknowledges support by the Czech Science Foundation through the project grant GACR 25-18493s : *Key to Cosmic Rays: A novel approach to a classical problem.* The authors gratefully acknowledge the computing time made available to them on the high-performance computer "Lise" at the NHR Center NHR@ZIB. This center is jointly supported by the Federal Ministry of Education and Research and the state governments participating in the NHR (www.nhr-verein.de/unsere-partner).

APPENDIX

A. POLARIZATION OF OBLIQUE WAVES

We define the polarization of waves by the fluctuating magnetic fields. With ω and $\mathbf{k}$ representing the wave frequency and the wavevector, a circularly polarized wave can be described as the sum of two linearly polarized waves,

$$\mathbf{B}(\mathbf{r},t) = B_0 e^{\imath(\mathbf{k}\cdot\mathbf{r}-\omega t)}[\hat{\mathbf{e}}_1 \mp \imath\,\hat{\mathbf{e}}_2], \tag{A1}$$

where $\hat{\mathbf{e}}_1$ and $\hat{\mathbf{e}}_2$ are unit vectors that, together with $\hat{\mathbf{k}}$, form a right-handed orthogonal set of unit vectors. The "+" sign in the above expression denotes a left-hand circularly polarized wave, while the "-" sign denotes a right-hand circularly polarized wave.

For a wave propagating along the x-axis in Cartesian coordinates, the orthogonal set of unit vectors $(\hat{\mathbf{e}}_1, \hat{\mathbf{e}}_2, \hat{\mathbf{k}})$ can be $(-\hat{\mathbf{z}}, \hat{\mathbf{y}}, \hat{\mathbf{x}})$. Since the wave is transverse, the magnetic-field vector has y and z components. Our simulations are performed in the xy plane, in which waves can have an arbitrary orientation $\mathbf{k} = (k_x, k_y)$. Rotating the coordinate system by the angle between the wavevector and the x-axis, $\theta(\mathbf{k}) = \angle(\mathbf{k}, \hat{\mathbf{x}}) = \arctan(k_y/k_x)$, gives

$$(\hat{\mathbf{e}}_1, \hat{\mathbf{e}}_2, \hat{\mathbf{k}}) = (-\hat{\mathbf{z}}, -\sin\theta\hat{\mathbf{x}} + \cos\theta\hat{\mathbf{y}}, \hat{\mathbf{k}}). \tag{A2}$$

The magnetic vector of a circularly polarized wave,

$$\mathbf{B}(\mathbf{r},t) = B_0 e^{\imath(\mathbf{k}\cdot r-\omega t)}[\pm\imath\sin\theta\hat{\mathbf{x}} \mp \imath\cos\theta\hat{\mathbf{y}} - \hat{\mathbf{z}}] = B_x\hat{\mathbf{x}} + B_z\hat{\mathbf{y}} + B_z\hat{\mathbf{z}}, \tag{A3}$$

can then be split into amplitudes for the right and left hand polarization,

$$B_R = B_z - \imath(B_x\sin\theta - B_y\cos\theta), \tag{A4}$$

$$B_L = B_z + \imath(B_x\sin\theta - B_y\cos\theta). \tag{A5}$$

For the right (left) hand polarization, B_R (B_L) equals $-2B_0 e^{\imath(\mathbf{k}\cdot r-\omega t)}$, while zero for the left (right) hand polarization.

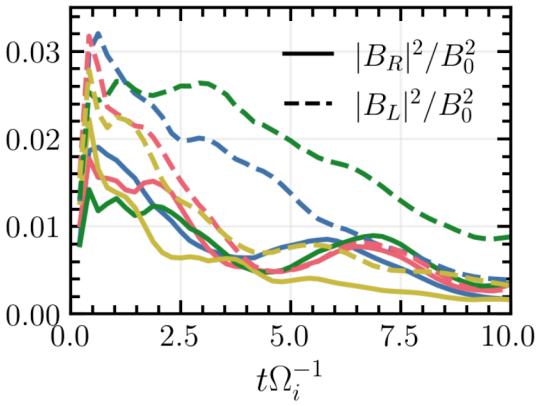


Figure 10. The evolution of the energy density of the right and left circularly polarized waves for different plasma slabs. The energy density is normalized to the energy density of the initial background magnetic field.

B. POLARIZATION MEASUREMENTS IN PRE-EXISTING TURBULENCE

In our shock simulations, the upstream medium consists of slabs of compressive turbulence, which are simulated separately in periodic box simulations and then injected into a shock simulation. To investigate the properties of wave modes in the electron foreshock, particularly their polarization, we first examine them in the pre-defined slabs of turbulent plasma. Figure 10 shows the evolution of the energy density in the right and left circularly polarized modes for four example plasma slabs, marked by different colors. The energy density is calculated using Equations 1 and 2. We typically inject slabs after the initial rapid period of evolution, at about $\Omega_i^{-1}t \approx 2$. At this stage B_L is stronger than B_R, but as the turbulence evolves, their magnitudes become comparable. To summarize, in the upstream region with pre-existing turbulence we expect to have $B_R^2 \sim B_L^2 \sim 0.01B_0^2$, which is consistent with the values in Figure 5.

REFERENCES

Amano, T., Matsumoto, Y., Bohdan, A., et al. 2022, Reviews of Modern Plasma Physics, 6, doi: 10.1007/s41614-022-00093-1

Arrò, G., Pucci, F., Califano, F., Innocenti, M. E., & Lapenta, G. 2023, ApJ, 958, 11, doi: 10.3847/1538-4357/acf12e

Axford, W. I., Leer, E., & Skadron, G. 1977, 15th International Cosmic Ray Conference, 11

Bagenal, F., Belcher, J. W., Sittler Jr., E. C., & Lepping Jr., R. P. 1987, Journal of Geophysical Research: Space Physics, 92, 8603, doi: https://doi.org/10.1029/JA092iA08p08603

Bell, A. R. 1978, Monthly Notices of the Royal Astronomical Society, 182, 147, doi: 10.1093/mnras/182.2.147

Blandford, R. D., & Ostriker, J. P. 1978, Astrophysical Journal, 221, L29, doi: 10.1086/182658

Bohdan, A. 2023, Plasma Physics and Controlled Fusion, 65, doi: 10.1088/1361-6587/aca5b2

Bohdan, A., Niemiec, J., Kobzar, O., & Pohl, M. 2017, The Astrophysical Journal, 847, 71, doi: 10.3847/1538-4357/aa872a

Bohdan, A., Weidl, M. S., Morris, P. J., & Pohl, M. 2022, Physics of Plasmas, 29, 052301, doi: 10.1063/5.0084544

Bresci, V., Lemoine, M., & Gremillet, L. 2023, Phys. Rev. Res., 5, 023194, doi: 10.1103/PhysRevResearch.5.023194

Brose, R., Pohl, M., & Sushch, I. 2021, A&A, 654, A139, doi: 10.1051/0004-6361/202141194

Carbone, F., Sorriso-Valvo, L., Khotyaintsev, Y. V., et al. 2021, Astronomy and Astrophysics, 656, doi: 10.1051/0004-6361/202140931

Demidem, C., Nättilä, J., & Veledina, A. 2023, The Astrophysical Journal Letters, 947, L10, doi: 10.3847/2041-8213/acc84a

Dubner, G., & Giacani, E. 2015, Radio emission from supernova remnants, Springer Verlag, doi: 10.1007/s00159-015-0083-5

Espinoza-Troni, J., Arrò, G., Asenjo, F. A., & Moya, P. S. 2025, The Astrophysical Journal, 986, 228, doi: 10.3847/1538-4357/add537

Fraternale, F., Adhikari, L., Fichtner, H., et al. 2022, Space Science Reviews, 218, doi: 10.1007/s11214-022-00914-2

Fulat, K., Bohdan, A., Torralba Paz, G., & Pohl, M. 2023, The Astrophysical Journal, 959, 119, doi: 10.3847/1538-4357/ad04dc

Guo, F., Giacalone, J., & Zhao, L. 2021, Frontiers in Astronomy and Space Sciences, 8, doi: 10.3389/fspas.2021.644354

Katou, T., & Amano, T. 2019, The Astrophysical Journal, 874, 119, doi: 10.3847/1538-4357/ab0d8a

Koyama, K., Petre, R., Gotthelf, E. V., et al. 1995, Nature, 378, 255, doi: 10.1038/378255a0

Krymskii, G. F. 1977, Soviet Physics Doklady, 22, 327

Kumar, N., & Reville, B. 2021, The Astrophysical Journal Letters, 921, L14, doi: 10.3847/2041-8213/ac30e0

Lee, K. H., & Lee, L. C. 2020, The Astrophysical Journal, 904, 66, doi: 10.3847/1538-4357/abba20

Madanian, H., Desai, M. I., Schwartz, S. J., et al. 2021, ApJ, 908, 40, doi: 10.3847/1538-4357/abcb88

Matsumoto, Y., Amano, T., Kato, T. N., & Hoshino, M. 2017, Physical Review Letters, 119, doi: 10.1103/PhysRevLett.119.105101

Morris, P. J., Bohdan, A., Weidl, M. S., & Pohl, M. 2022, The Astrophysical Journal, 931, 129, doi: 10.3847/1538-4357/ac69c7

Morris, P. J., Bohdan, A., Weidl, M. S., et al. 2023, The Astrophysical Journal, 944, 13, doi: 10.3847/1538-4357/acaec8

Niemiec, J., Pohl, M., Stroman, T., & Nishikawa, K. 2008, The Astrophysical Journal, 684, 1174, doi: 10.1086/590054

Ocker, S. K., Cordes, J. M., Chatterjee, S., & Dolch, T. 2021, The Astrophysical Journal, 922, 233, doi: 10.3847/1538-4357/ac2b28

Orlando, S., Miceli, M., Ustamujic, S., et al. 2021, New Astronomy, 86, doi: 10.1016/j.newast.2020.101566

Orusa, L., & Valenzuela-Villaseca, V. 2025, Physics of Plasmas, 32, 052901, doi: 10.1063/5.0269035

Perri, S., Bykov, A., Fahr, H., Fichtner, H., & Giacalone, J. 2022, Space Science Reviews, 218, doi: 10.1007/s11214-022-00892-5

Pohl, M. 1996, A&A, 307, L57, doi: 10.48550/arXiv.astro-ph/9602115

Pohl, M., Hoshino, M., & Niemiec, J. 2020, Progress in Particle and Nuclear Physics, 111, doi: 10.1016/j.ppnp.2019.103751

Raymond, J. C., Ghavamian, P., Bohdan, A., et al. 2023, The Astrophysical Journal, 949, 50, doi: 10.3847/1538-4357/acc528

Reynolds, S. P. 2008, Annual Review of Astronomy and Astrophysics, 46, 89, doi: https://doi.org/10.1146/annurev.astro.46.060407.145237

Shi, Q., Yao, S., Hamrin, M., & Liu, J. 2024, Science China Earth Sciences, 67, 2739, doi: 10.1007/s11430-023-1290-8

Shklovsky, J. S. 1954, Liege International Astrophysical Colloquia, 5, 515. https://ui.adsabs.harvard.edu/abs/1954LIACo...5..515S

Slavin, J. A., Smith, E. J., Spreiter, J. R., & Stahara, S. S. 1985, Journal of Geophysical Research: Space Physics, 90, 6275, doi: https://doi.org/10.1029/JA090iA07p06275

Sulaiman, A. H., Masters, A., & Dougherty, M. K. 2016, Journal of Geophysical Research (Space Physics), 121, 4425, doi: 10.1002/2016JA022449

Sulaiman, A. H., Masters, A., Dougherty, M. K., et al. 2015, PhRvL, 115, 125001, doi: 10.1103/PhysRevLett.115.125001

Sundberg, T., Burgess, D., Scholer, M., Masters, A., & Sulaiman, A. H. 2017, The Astrophysical Journal Letters, 836, L4, doi: 10.3847/2041-8213/836/1/L4

Tomita, S., Ohira, Y., & Yamazaki, R. 2019, The Astrophysical Journal, 886, 54, doi: 10.3847/1538-4357/ab4a10

Trotta, D., Valentini, F., Burgess, D., & Servidio, S. 2021, Proceedings of the National Academy of Sciences of the United States of America, 118, doi: 10.1073/pnas.2026764118

Trotta, D., Pezzi, O., Burgess, D., et al. 2023, Monthly Notices of the Royal Astronomical Society, 525, 1856, doi: 10.1093/mnras/stad2384

Vink, J. 2012, Astronomy and Astrophysics Review, 20, doi: 10.1007/s00159-011-0049-1

Wang, X., Filippenko, A. V., Ganeshalingam, M., et al. 2009, ApJL, 699, L139, doi: 10.1088/0004-637X/699/2/L139

Wieland, V., Pohl, M., Niemiec, J., Rafighi, I., & Nishikawa, K.-I. 2016, The Astrophysical Journal, 820, 62, doi: 10.3847/0004-637x/820/1/62

Xu, R., Spitkovsky, A., & Caprioli, D. 2020, The Astrophysical Journal Letters, 897, L41, doi: 10.3847/2041-8213/aba11e

Zhang, H., & Zong, Q. 2020, Transient Phenomena at the Magnetopause and Bow Shock and Their Ground Signatures (American Geophysical Union (AGU)), 11–37, doi: https://doi.org/10.1002/9781119509592.ch2

Zhang, H., Zong, Q., Connor, H., et al. 2022, Space Science Reviews, 218, 40, doi: 10.1007/s11214-021-00865-0